ELSEVIER

Physica B 201 (1994) 217–226

PHYSICA B

Research in semi-continuous high magnetic fields

J.J.M. Franse*, F.R. de Boer, P.H. Frings, A. de Visser

Van der Waals–Zeeman Laboratory, University of Amsterdam, Valckenierstraat 65, 1018 XE Amsterdam, The Netherlands

Abstract

An overview is presented of the main recent developments in the areas of research in the 40 T High Field Facility at the University of Amsterdam. In addition, the recent progress concerning the available sample environments for experiments in the facility are discussed.

1. Introduction

The University of Amsterdam explores an installation for semi-continuous magnetic fields that produces magnetic fields up to 40 T with a total duration of about 1 s. By means of a thyristor-based power-control system, a large flexibility in field–time profiles can be realised. Stepwise pulses can be generated with field levels constant within 10^{-4} during 100 ms. Also linearly increasing and decreasing fields as well as exponentially ripple-free decreasing fields belong to the standard field profiles that are frequently used in studies of magnetization, magnetoresistance, Hall effect, de Haas–van Alphen effect, Shubnikov–de Haas oscillations, relaxation phenomena, etc. Temperatures at which experiments can be performed range from 400 mK to room temperature. Hydrostatic pressures up to 5 kbar can be applied in the high-field magnetization and magnetoresistance studies. For more details about the facility see Refs. [1–3].

In the present paper, we shall review the latest results in the main areas of the high-field research in Amsterdam.

* Corresponding author.

2. Available sample environments in the 40 T installation

In the Amsterdam High Field Facility, experiments can be performed from 400 mK to room temperature. In the standard way, the measurements are carried out on samples immersed in (pumped) liquid ^{4}He, i.e. between 1.4 and 4.2 K. In the same ^{4}He bath cryostat, a variable-temperature insert can be mounted for measurements up to room temperature. Temperatures below 1 K are reached within a simple ^{3}He insert that also fits into the bath cryostat with an inner diameter of 15 mm. ^{3}He gas is condensed by contact with a stainless-steel wall of the ^{4}He cryostat and collected in the lower part of the ^{3}He insert which is a tube constructed of Kapton surrounded by a permanent vacuum space. The total amount of 3 cm^3 of liquid ^{3}He is subsequently pumped by an external rotary pump to reach a lowest temperature of 400 mK in about 30 minutes. The base temperature can be kept for several hours. Samples for magnetotransport measurements are mounted in the ^{3}He space on a Kapton tube together with a RuO_2 thermometer. Copper and manganin wires are used as current and voltage leads, respectively. Hall-effect measurements have been performed with this setup on a monocrystalline sample (dimensions $4 \times 2 \times 0.1$ mm^3) of URu_2Si_2 with the field along the tetragonal axis and perpendicular to the large surface of the sample. It turned out that the heating of the

SSDI 0921-4526(94)00062-Z

sample and the ^{3}He bath during a 40 T pulse is about 10 mK at the base temperature of 400 mK.

Measurements under hydrostatic pressure in the 40 T installation at liquid helium temperatures are performed in a copper–beryllium pressure vessel with helium as the pressure transmitting medium. The pressure vessel is connected by a flexible 1 mm diameter stainless-steel capillary (0.15 mm inner diameter) with a pressure generating unit which is at room temperature. Pressures are applied at temperatures where the helium gas does not solidify (around 40 K for pressures of 5 kbar). In order to keep pressures as high as possible in the solid-helium state, a temperature gradient is created during the helium-gas inlet so that the solidification of the helium gas starts at the bottom of the pressure vessel. Meanwhile, the capillary which is connected to the upper part of the pressure vessel, is heated in order to prevent a blocking of the narrow capillary. In this way the solidification takes place at constant pressure over the whole inner volume of the high-pressure vessel. Upon cooling down, the capillary is blocked and constant-volume conditions cause a drop in pressure which is measured by calibrated strain gauges at the outer side of the pressure vessel. In view of the limited space in the ^{4}He cryostat, two different types of pressure vessels have been constructed. The pressure vessel for magnetotransport measurements has an outer diameter of 14 mm and an inner diameter of 5 mm over a length of 25 mm. Four electrical leads are led through a capillary (1 mm inner diameter in this case) to a feedthrough that is kept at room temperature. An experimental problem one has to deal with at using a metallic pressure vessel in pulsed magnetic fields is the generation of eddy currents. Eddy currents will heat up the vessel and produce a small field opposite to the applied field. In order to keep the eddy-current heating under control, linearly increasing fields up to 28 T have been employed with rather small dB/dt values of 20 T/s. During these field sweeps, the temperature does not rise more than a few tenths of a degree above the temperature of the liquid-helium bath. A typical trace of a high-field high-pressure magnetotransport measurement is shown in Fig. 1 for the heavy-fermion compound UPt_3. To perform high-field magnetization measurements under hydrostatic pressures, a second pressure vessel has been constructed that fits into a pick-up coil system. It has an outer diameter of 5 mm and an inner diameter of 1.7 mm over a length of 40 mm. Samples are positioned in the center of the sample space by teflon spacers. The magnetization is measured by an induction method, i.e. by integrating the voltage induced in the pick-up coil during the field sweep. The pick-up coil has been constructed according to a design by Gersdorf et al. [4] and consists of two confocal concentricellipsoidal coils. The induced voltage is in good approximation insensitive to the exact position of the sample and to the external field. Eddy currents contribute in this case to the measured magnetization. This contribution is determined separately in a measurement without a sample, see Fig. 2. Due to the reduced dimensions, the eddy-current heating is less serious but still present. Again, by sweeping the field in a linear way with field-sweep rates below 20 T/s, the temperature excursion remains limited. In Fig. 3, a magnetization measurement is shown for the compound UPd_2Al_3 in a field sweep up to 28 T with a rate of 20 T/s under an applied pressure of 4 kbar. For further details the reader is referred to Ref. [5].

3. Selected research topics

3.1. Exchange interactions and magnetic anisotropies in R–T intermetallics

Recently, an experimental method has been developed [6, 7] to measure directly the 3d–4f coupling strength between the rare-earth and 3d magnetic moments in heavy rare-earth – 3d intermetallics. The method consists of high-field magnetization measurements on monocrystalline particles that are free to be oriented by the applied magnetic field. In its simplest form, the analysis of these experiments assumes a negligible magnetic anisotropy of the 3d element compared to that of the rare-earth element. The magnetization curves of a large number of these intermetallic compounds have successfully been described within molecular-field models by assuming two magnetic sublattices corresponding with the rare-earth and the 3d sublattices with a magnetic coupling between the two sublattices that is represented by the molecular-field coefficient n_{RT}. The freedom of the particle to orient itself in the applied field guarantees the rare-earth moment to be oriented along its easy direction in the crystal. In the limiting case of zero 3d anisotropy, the magnetization curve is described by the two sublattice magnetizations M_T and M_R, the angle α between these magnetization vectors, the molecular field coefficient, n_{RT}, and the applied magnetic field. Three different solutions are found: below a first critical field, $B_{cr,1} = n_{RT}|M_T - M_R|$, a strict antiparallel configuration of the sublattice moments is found with $M = |M_T - M_R|$. Above a second critical field $B_{cr,2} = n_{RT}(M_T + M_R)$, the two magnetic moments are parallel ($M = M_T + M_R$). In between these two critical fields, the magnetization depends strictly linearly on the applied field: $M = B/n_{RT}$. The validity of the method has been checked in detail on the compound Ho_2Co_{17} for which essentially the same magnetization curves were obtained for a monocrystalline sphere which

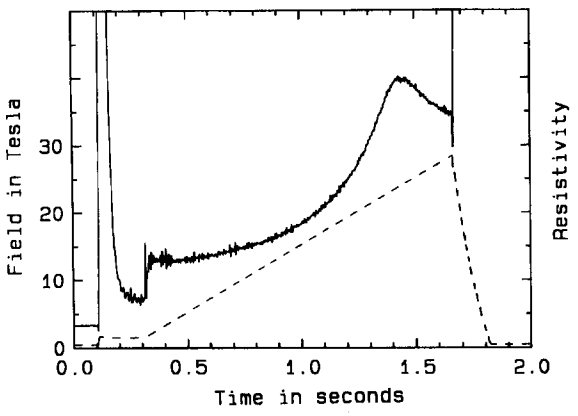

Fig. 1. Typical trace of a high-field high-pressure magnetoresistance measurement. The dashed curve represents the field profile (left scale). The solid curve represents the magnetoresistance of single-crystalline UPt_3 with both current (400 mA) and field along the a-axis (right scale). The pressure equals 4 kbar and the temperature 2 K.

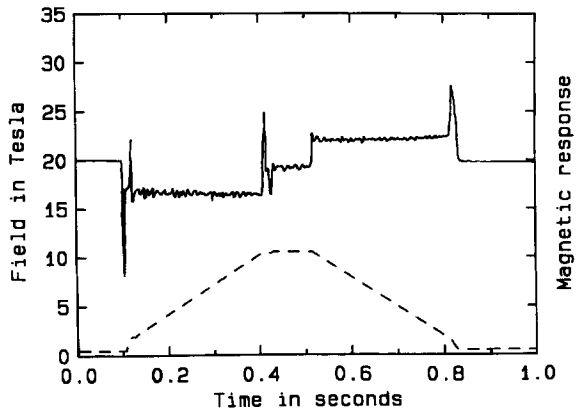

Fig. 2. Typical example of the magnetization signal obtained from the empty pressure vessel before removal of the eddy-current signal. The dashed curve represents the field profile (left scale). The solid curve represents the magnetization signal (right scale).

was free to rotate in the applied field and for free powder particles with a size smaller than 30 micron, obtained by crushing polycrystalline material. In recent years, a large variety of series of R–T compounds with R = Gd, Tb, Dy, Ho, Er, Tm and T = Fe, Co, Ni has been investigated in the Amsterdam High Field Facility by means of the free-powder technique. This has provided a good insight in the variation of the R–T interaction within and between series of R–T intermetallics [8]. In general, chemical substitutions have to be carried out which make the R- and T-sublattice magnetizations more similar, so that the values of the critical field $B_{cr,1}$ are brought within the experimentally accessible field window of 40 T. In Fig. 4, the free-powder magnetization of $DyCo_{12}B_6$ [9] is shown. This is an exceptionally nice example which exhibits the full scala of moment configurations described above without any chemical substitution being necessary. It has been noticed by Zhao et al. [10–12] that sometimes the strict linearity in the intermediate field range does not hold. An example is found in the magnetization curve of a free monocrystalline sphere of the hexagonal compound Er_2Fe_{17} [13] (Fig. 5), an easy-plane system due to the relatively weak Er, anisotropy and the dominant Fe anisotropy. Beyond $B_{cr,1}$, a modulation is found on the linear magnetization. A more clear example of this behaviour is found for the easy-plane tetragonal compound $ErCo_{10}Si_2$ [14] (Fig. 6). Zhao et al. [12] have shown that these slight oscillatory deviations are due to magnetic anisotropies that have been neglected in the above-given analysis. From an elaborate

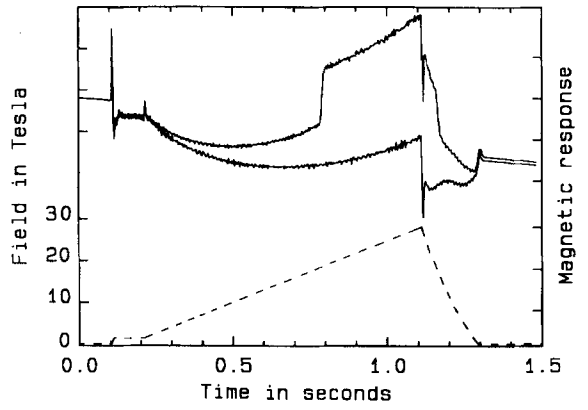

Fig. 3. Trace of a magnetization measurement with removal of the eddy-current signal. The dashed curve represents the field profile (left scale). The upper solid curve represents the magnetization measurement of UPd_2Al_3 ($B \| a$) at a pressure of 4 kbar. The lower solid curve represents the magnetization of the empty pressure vessel. By subtracting the lower curve from the top curve, the magnetization of the sample is obtained. The overall decrease of the signal with increasing time is caused by the drift of the integrator.

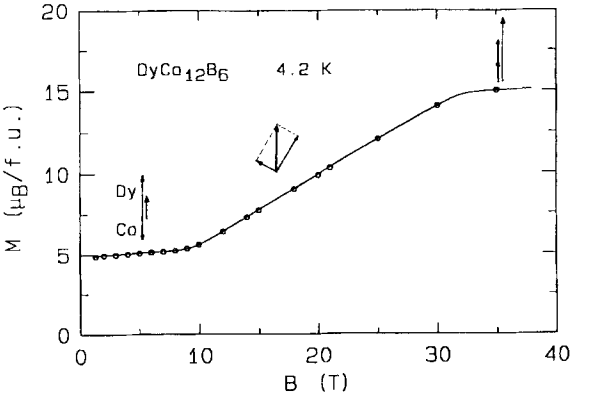

Fig. 4. Free-powder magnetization curve at 4.2 K of $DyCo_{12}B_6$ [9]. The circles represent measurements in quasi-stationary fields and the full line corresponds to a measurement in a field decreasing linearly with time at a rate of 50 T/s. The moment configurations in the different field intervals are indicated.

analysis, the magnetization for an easy-plane tetragonal compound in the intermediate field region is found to satisfy the relation

$$B/M = n_{RT} - 16\,K_{4T}\cos\alpha\cos 2\alpha(1 - K_{4T}\cos 4\alpha/K_{4R})/M_R M_T$$

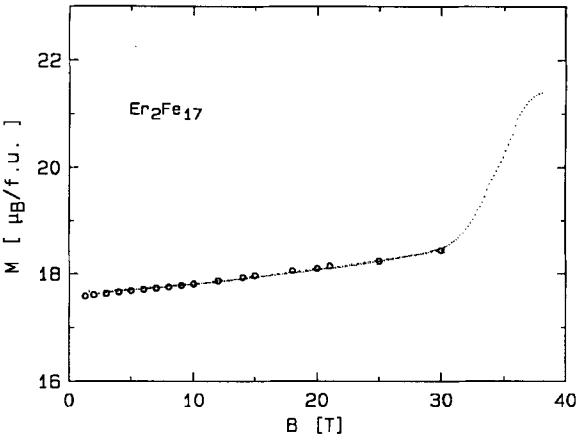

Fig. 5. Magnetization at 4.2 K of a spherical Er_2Fe_{17} single crystal free to rotate in the applied magnetic field [13]. The circles represent measurements in quasi-stationary fields and the dotted line corresponds to a measurement in a field increasing in an uncontrolled way and decreasing linearly with time at a rate of 50 T/s.

where K_4 is the in-plane anisotropy constant. For K_{4T} equal to zero, the equation is reduced to the simple form $M = B/n_{RT}$, discussed above. For further details the reader is referred to the forthcoming paper by Zhao et al. [12].

3.2. Hybridization effects in uranium compounds

Uranium compounds are known for their extremely large magnetic anisotropies and for the sometimes very complex magnetic phase diagrams. In the past years, high-field magnetization measurements have proven to be a powerful tool in studying the role of hybridization in the formation of localized uranium 5f moments and in the magnetic anisotropy. In a systematic investigation of isostructural UTX (T = transition metal and X = p-electron element) compounds, a clear trend from itinerant 5f-electron behaviour to localized 5f moments was established with decreasing 5f-ligand hybridization [15]. It was also found that, as a rule, the strong magnetocrystalline anisotropy orients the uranium moments perpendicular to the shortest inter-uranium distance [16]. Recently, the systematic study of hybridization effects in uranium intermetallics was extended [17] to the newly discovered group of isostructural U_2T_2X compounds, which crystallize in the tetragonal U_3Si_2 structure [18, 19]. Investigation of this family of compounds is of particular interest since, depending on the constituting elements T and X, the shortest inter-uranium distance in

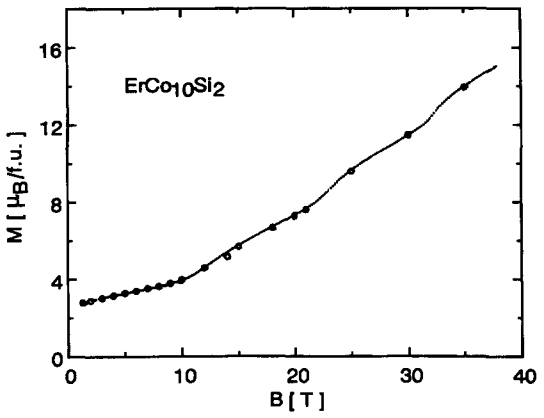

Fig. 6. Free-powder magnetization curve at 4.2 K of $ErCo_{10}Si_2$ [14]. The circles represent measurements in quasi-stationary fields and the dotted line corresponds to a measurement in a field decreasing linearly with time at a rate of 50 T/s.

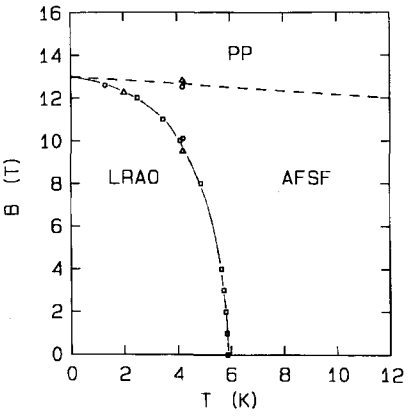

Fig. 7. The magnetic phase diagram of $U(Pt_{0.95}Pd_{0.05})_3$ for $B \| a$. Data are taken from specific heat (□), magnetization (△) and magnetoresistance (○). LRAO denotes long-range antiferromagnetic order, AFSF denotes antiferromagnetic short-range correlations and PP denotes the polarised paramagnetic state.

these compounds is found either within the basal plane or along the c axis.

3.3. *Critical fields in heavy-fermion systems*

The heavy-fermion behaviour in some specific cerium and uranium compounds points to a strongly correlated electron gas leading to large values for the coefficient of the electronic term in the specific heat, to spin-fluctuation and/or Kondo-type of behaviour in the resistivity, to coherence effects, to long-range or short-range magnetic order and in some cases to superconductivity. Each of these phenomena can be represented by a characteristic temperature and magnetic field. Frequently, a direct relation between the characteristic temperature and field is found. In UPt_3, for instance, the maximum in the low-field $\chi_{ab}(T)$ curve at 17 K is related to the maximum in the low-temperature $\chi_{ab}(B)$ curve at 20 T according to $k_B T_{max} \approx \mu_B B_{max}$. In the $\chi_{ab}(T)$ curve of UPt_3, deviations from Curie–Weiss behaviour already start below 50 K, suggesting that for a full suppression of the heavy-fermion state in this compound magnetic fields in the range of 100 T are required. In the present paper, the low-temperature magnetic phase diagrams of the heavy-fermion compounds $U(Pt_{0.95}Pd_{0.05})_3$ and UPd_2Al_3 are discussed.

Long-range antiferromagnetic order can be introduced in UPt_3 by substituting 5% of the platinum atoms by iso-electronic palladium atoms [20, 21]. The ordering temperature is 5.8 K and the moment per uranium atom is about $0.5\mu_B$. Low-temperature specific-heat studies show increased values for the electronic-mass enhancement compared to UPt_3. The metamagnetic transition, as observed in magnetization measurements, is found at 20 T for UPt_3 but is shifted to the lower value of 13 T for $U(Pt_{0.95}Pd_{0.05})_3$. In fact, magnetoresistance studies reveal two anomalies for the latter compound: a relatively pronounced maximum at the metamagnetic transition field that remains visible at temperatures well above 10 K and a weaker anomaly at lower field values that disappears above 5.8 K. The weaker anomaly corresponds with the pronounced peaks in the specific heat which indicate the onset of long-range antiferromagnetic order upon cooling. These observations have led to the magnetic phase diagram of $U(Pt_{0.95}Pd_{0.05})_3$ [22] that is shown in Fig. 7. The phase diagram suggests that there is no direct transition from the long-range antiferromagnetic state to the polarised paramagnetic state but that there is an intermediate state with short-range antiferromagnetic correlations characterized by a weakly temperature dependent critical field of about 13 T. Evidently, the two extrapolated phase lines meet at zero temperature. For a study of the nature of the short-range antiferromagnetic correlations, the relevant question is whether at zero temperature this intermediate state can exist in $U(Pt_{0.95}Pd_{0.05})_3$. To answer this question, high-field high-pressure magnetoresistance measurements have been performed on this peculiar compound. These experiments were motivated by the following considerations: in UPt_3, high-field high-pressure experiments have shown that the metamagnetic field shifts to higher field values under pressure with a rate of 0.60 T/kbar [23]; high-pressure resistivity studies by Van Sprang, on the other hand, have shown that the long-range antiferromagnetic order in $U(Pt_{0.95}Pd_{0.05})_3$ is depressed with

pressure, pointing to a depression of the long-range-order transition field with pressure [24]. In Figs. 8(a) and (b), the magnetoresistance data are collected at ambient pressure for $T = 2.0$ K and 4.2 K and at applied pressures for $T = 2.0$ K, respectively. The experiments clearly show a splitting of the magnetoresistance maximum at 2.0 K in two distinct anomalies under pressure and give a clear answer to the above-formulated question.

The heavy-fermion compound UPd_2Al_3 attracts much attention because of the coexistence of superconductivity ($T_c = 2$ K) and long-range antiferromagnetic order ($T_N = 14.4$ K) [25]. Recent experiments revealed that the superconducting [26] and antiferromagnetic [27] phase diagrams consist of a multiplicity of phases. In the case of the superconducting phase diagram this was attributed to the possible formation of a novel Fulde–Ferrell state. As regards the antiferromagnetic phase diagram three

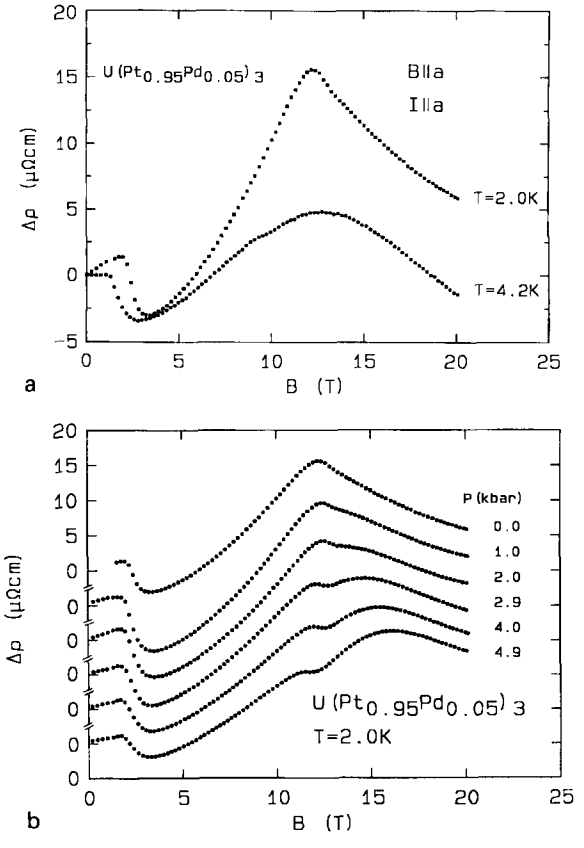

Fig. 8. (a) The magnetoresistance data for $U(Pt_{0.95}Pd_{0.05})_3$ for $B \| I \| a$ at 2.0 K (■) and 4.2 K (●). (b) Magnetoresistance data for $U(Pt_{0.95}Pd_{0.05})_3$ for $B \| I \| a$ at 2.0 K under hydrostatic pressures up to 4.9 kbar as indicated.

different phases with critical fields $B_1 = 0.6$ T [27], $B_2 = 4.2$ T [27] and $B_3 = 18$ T [28, 29] (for $B \perp c$ and $T \to 0$) have been reported, which suggests that the suppression of the long-range antiferromagnetic order takes place in a three-step process. In the high-field magnetization, $M(B)$, measured at 1.3 K and 4.2 K [28], the antiferromagnetic phase boundary shows up as a sharp jump ($\Delta M = 0.94\ \mu_B$/U-atom) at $B_{af} = B_3$. In the transversal, $\rho_\perp(B)$, and longitudinal, $\rho_\parallel(B)$, magnetoresistance, B_{af} appears as a sudden drop and as a pronounced peak, respectively [29]. The critical fields B_1 and B_2 have been distinguished by susceptibility, magnetoresistance and magnetostriction experiments [27]. Zero-field neutron-diffraction experiments [30] have shown that the ordered moment amounts to $0.85 \pm 0.03\ \mu_B$/U-atom ($\simeq \Delta M$ at B_{af}). The ordering consists of ferromagnetic sheets parallel to the basal plane, which are coupled antiferromagnetically along the hexagonal (c-)axis, i.e. a doubling of the nuclear unit cell with an ordering vector $\boldsymbol{k} = [0, 0, \frac{1}{2}]$. However, the in-plane orientation of the ordered moment and the magnetic structures of the field-induced phases have not yet been resolved.

Recently, we have investigated the antiferromagnetic phase diagram in more detail by means of magnetoresistance experiments [31]. In Fig. 9 we show $\rho_\perp(B)$ for $I \| c$ and $B \| a$ over a wide temperature interval ($3.68\ \text{K} < T < 19.5$ K). These experiments have been carried out in static fields at the Nÿmegen High Field Magnet Laboratory. B_{af} appears as a sharp drop at the lowest temperatures. However, a small but significant anisotropy is found: B_{af} equals 18.4 T and 17.8 T for $B \| a$ and $B \| b$, respectively (we take $a \perp b$). At higher temperatures the anomaly at B_{af} develops into a well defined maximum. A second anomaly is found at lower fields (B_2) but only for $B \| a$, evidencing a pronounced basal-plane anisotropy. This was confirmed by in-situ rotation of the sample around the c-axis in a field of 5 T. In Fig. 10, we have traced B_2 and B_{af} as function of temperature. The lower phase line (dashed line in Fig. 10) is likely caused by the reorientation of the antiferromagnetic domains, as to form a mono-domain sample. When increasing the field further, one expects the moments to align perpendicular to the field (spin-flop). The fact that such a transition is not observed for $B \| b$ (the middle phase line is absent) strongly suggest that the zero-field moments are directed along the a-axis (in which case they are already oriented perpendicular to B). However, for the configuration $B \| a$ a spin-flop towards the b-axis (the middle phase line) will take place. Finally, at B_3 the antiferromagnetic order is suppressed.

The phase diagram (Fig. 10) contrasts with the one proposed by Sugiyama et al. [32] obtained by high-field magnetization experiments. These authors claimed the existence of a nearly-temperature independent phase

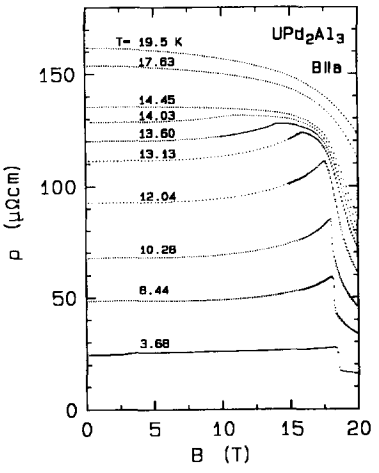

Fig. 9. Transversal magnetoresistance ($I \| c$) of UPd_2Al_3 for $B \| a$ at temperatures as indicated.

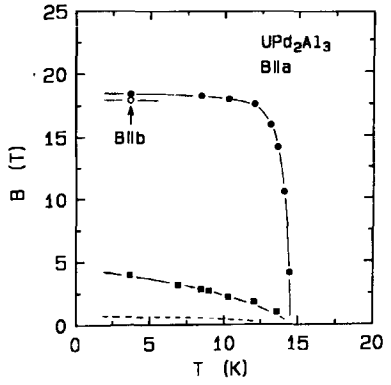

Fig. 10. Antiferromagnetic phase diagram of UPd_2Al_3 for $B \| a$. The dashed line is taken from Ref. [27]. The open circle denotes the antiferromagnetic phase boundary for $B \| b$. The middle phase line (closed squares) is absent for $B \| b$.

line (up to ~ 30 K) at a field $B_3 \approx 18$ T. It is likely, however, that the transition fields obtained in Ref. [32] for temperatures just below T_N and above are connected to a gradual suppression of the magnetic fluctuations persisting for $T \geq T_N$ and $B \geq B_{af}$, as inferred from the steady decrease of $\rho_\perp(B)$ at high-fields and high-temperatures (Fig. 9).

3.4. Critical currents and upper critical fields in high-T_c superconductors

High-field installations have shown their importance in the study of high-T_c superconductors in particular. Upper critical fields in the cuprate superconductors turn out to be extremely large, critical currents in large fields were found to exceed those of the conventional superconductors. The very large values of the critical-current density, J_c, at low temperatures make it experimentally difficult to directly measure the critical current on bulk single-crystalline samples by transport measurements. Indirectly, the critical current can be deduced form the irreversible magnetization on the basis of the Bean critical-state model [33]. In a previous report [34], the effect of the field-sweep rate on the magnetization curve has been discussed. An important conclusion of this previous report is that the flux-line profile under rapidly varying magnetic fields depends on the field-sweep rate. For the compound $(La, Sr)_2CuO_4$, three types of behaviour have been identified: a stable regime for low field-sweep rate (below 1 T/s) fitting into the critical-state model; an intermediate regime (between 1 and 10 T/s) with periodic instabilities and a second stable regime with reduced values for the irreversible magnetization at higher sweep rates. In the set of high-field experiments on a collection of single-crystalline samples of the compound $YBa_2Cu_3O_7$ [35], magnetization data have been taken at field-sweep rates between 40 and 140 T/s. In this range of sweep-rate values, no effect on the irreversible magnetization is observed. Application of the Bean critical-state model, however, may not be justified.

Nevertheless, the irreversible magnetization data have been used to calculate the critical-current density as a function of the applied field for different temperatures following the Bean model. Subsequently, the volume density of the pinning force, F_p, can be deduced according to the expression: $\boldsymbol{F}_p = \boldsymbol{J}_c \times \boldsymbol{B}$. For fields parallel to the c-axis, the pinning force is plotted in Fig. 11 at high temperatures in a plot of F_p/F_p^{max} versus B/B_0, where F_p^{max} is the maximum value of $F_p(B)$ at a given temperature and where B_0 denotes the field where the irreversibility in the magnetization disappears. This latter field is not necessarily equal to the upper critical field B_{c2}, since flux-flow phenomena may cause B_0 to be smaller than B_{c2}. Experimentally it is found that $F_p^{max}(T)$ and $B_0(T)$ follow the relation: $F_p^{max}(T) = 2.7 \times 10^6\ [B_0(T)]^{2.5}$ [35]. The high-temperature data can be scaled very well with the following expression [35]: $F_p(T)/F_p^{max}(T) = 45.6\ b^2(1-b)^4$ with $b = B/B_0$, see the solid curve in Fig. 11. Consequently, we can write: $F_p(T, B) = 1.23 \times 10^8\ [B_0(T)]^{2.5}\ b^p(1-b)^q$ [35]. This expression resembles the expression for the temperature and field dependence of the pinning force for conventional superconductors which is given by the Kramer scaling formula that differs from this expression by B_{c2} taking the place of B_0. In the model forwarded by Kramer [36], the pinning force is determined by two contributions: the pinning strength of line pins and the shear strength of the flux-line lattice. At low fields, flux motion occurs by depinning of

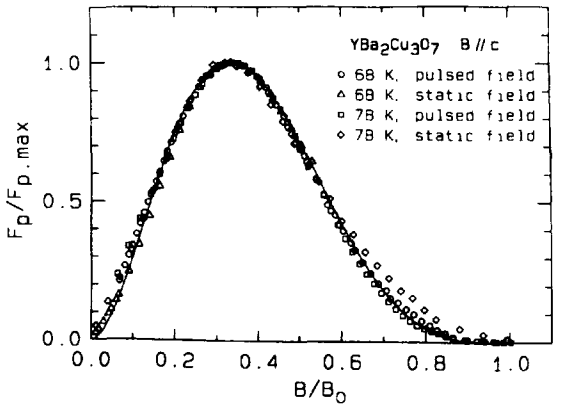

Fig. 11. Plot of the normalised pinning force F_p/F_p^{max} versus the normalised field B/B_0. The full curve is a fit to the experimental data, see text.

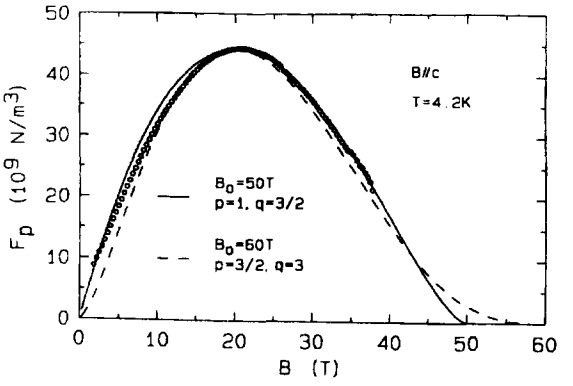

Fig. 12. Fits of the F_p data at low temperature with various values of B_0, p and q, see text.

line pins, whereas at high fields it occurs by a synchronous shear of the flux lines around strong line pins which causes the pinning force to follow a $(1-b)^2$ dependence as observed, for instance, for Nb_3Sn [37]. The high-temperature behaviour, shown in Fig. 11, follows a higher power of $(1-b)$ ($q=4$) which seems to imply that the elastic properties of the flux-line lattice of $YBa_2CU_3O_7$ at higher temperatures are different from those of conventional type-II superconductors. The data at low temperature cannot be analysed in a straightforward manner since the irreversibility field cannot be reached in experiments up to 40 T. By assuming that the above-given relation between $F_p^{max}(T)$ and $B_0(T)$ holds, a value of 50 T is found for B_0 at 4.2 K. The full curve in Fig. 12 is the result of a fitting to the experimental data giving $p=1$ and $q=1.5$. The broken curve is determined by another set of parameters: $B_0=60$ T, $p=1.5$ and $q=3$. The two fitted curves give a feeling for the boundaries of the parameter space. Anyhow it is clear that the field dependence of F_p at lower temperatures is closer to a $(1-b)^2$ relation than at higher temperatures, indicating that the elastic properties of the flux-line lattice in $YBa_2Cu_3O_7$ at lower temperature better resembles that of conventional type-II superconductors. Further details of this analysis can be found in Ref. [38].

3.5. *Acceptor type graphite intercalation compounds*

The intercalation of graphite provides a powerful technique for the controlled variation of materials parameters [39]. Over the past decade, a wide variety of graphite intercalation compounds (GIC) has been synthesized and characterized. GIC display a number of interesting physical phenomena, among which superconductivity and magnetic order. Besides, GIC offer ample possibilities to study charge transport in quasi-two-dimensional structures. The physical characteristics depend on many factors, like the nature of the intercalant (acceptor or donor type), the stage number (i.e. the number of graphite layers between the nearest intercalant layers) and the method of synthesis.

Acceptor-type GIC may be synthesized by the interaction of halogens, interhalides, metal halides or acids. One of the fascinating properties of acceptor-type GIC is that they may have a very high electrical conductivity (in the hexagonal basal-plane) at room temperature, which, in combination with a low specific weight, makes them potentially attractive for applications. Detailed knowledge of the electronic band structure of GIC is of great importance for the explanation of the high conductivity and for the controlled search for novel GIC with desirable physical properties. Comprehensive information about the band structure, the Fermi surface, the effective masses and the carrier concentration is provided by the investigation of magnetic quantum oscillations at low temperatures.

A significant research effort into this field has been made by Kulbachinskii and coworkers [40–42], who investigated the Shubnikov–de Haas (SdH) effect for a large number of low-stage GIC, among which mono-intercalated compounds, like the stage-1 compounds $C_{9.3}AlCl_{3.4}$, $C_{9.5}AlCl_3Br_{0.6}$ and $C_8H_2SO_4$, and the stage-2 compounds $C_{9.8}CuCl_2$, $C_{27.5}ICl_3$, $C_{12}FeCl_3$, $C_{18.6}AlCl_{3.4}$ and $C_{16.3}ICl_{1.1}$ and hetero-intercalated compounds, like the stage-1 compound $C_{10}CuCl(ICl)_{0.6}$ and the stage-2 compound $C_{12}FeCl_3(ICl)_{0.75}$. Recently, we have investigated the SdH effect of some selected stage-2 GIC compounds in high magnetic fields ($B<35$ T).

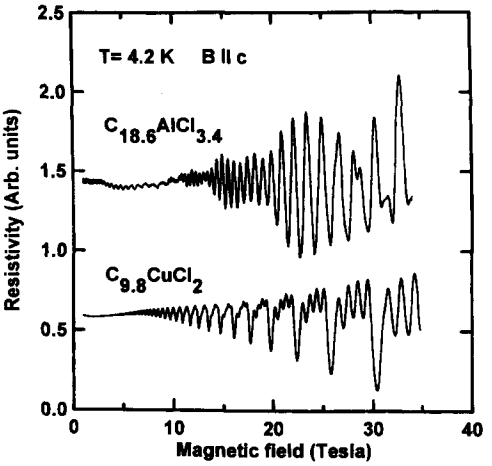

Fig. 13. Shubnikov–de Haas oscillations for stage 2 graphite intercalation compounds for B along the hexagonal axis (at 4.2 K).

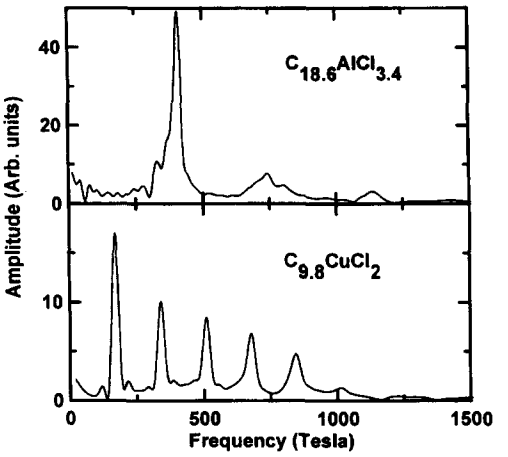

Fig. 14. Fourier transform of the Shubnikov–de Haas signal for the compounds as indicated (at 4.2 K).

The samples were prepared by the intercalation of highly-oriented pyrolytic graphite. The pure graphite, annealed at a temperature of 3300 K, is characterized by a basal-plane grain size of $\sim 10^5$ Å, a mosaic spread of less than 1° with respect to the hexagonal axis (c-axis). For details on sample preparation and characterization we refer to Ref. [42]. The high quality of the prepared single-crystalline specimens is assured by the detection of magnetic quantum oscillations. The samples had plate-like shapes with typical dimensions $5 \times 1 \times 0.5$ mm^3 (the c-axis is directed normal to the surface of the plate). Transverse magnetoresistance measurements were performed, using standard four-point techniques, for a current directed in the basal plane and a magnetic field applied along the c-axis.

For all investigated mono-intercalated stage-2 compounds, the low-field data ($B < 6$ T) revealed a single SdH frequency, while the angular dependence of the extremal cross-section indicated a nearly cylindrical Fermi surface. However, in high-magnetic fields the SdH oscillations revealed additional features, i.e. spin-splitting and frequency beats. Some typical resistivity versus magnetic field traces for $C_{18.6}AlCl_{3.4}$ and $C_{9.8}CuCl_2$ taken at $T = 4.2$ K are shown in Fig. 13. The Fourier transforms of the signals are shown in Fig. 14. The extremal cross section of the Fermi surface amounts to 372×10^{12} cm^{-2} and 163×10^{12} cm^{-2}, while the effective mass (m^*) amounts to $0.15m_e$ and $0.09m_e$, for the intercalants $AlCl_{3.4}$ and $CuCl_2$, respectively. The carrier (hole) concentration, calculated from the SdH data, amounts to 2.9×10^{20} cm^3 and 1.3×10^{20} cm^3, respectively. The frequency beats observed for $C_{18.6}AlCl_{3.4}$ indicate the presence of two close frequencies of different amplitude in each harmonic. One of the reasons for this might be a Fermi surface consisting of an undulating cylinder with two extremal cross sections in the center of the Brillouin zone boundary, which suggests the presence of an interaction between the carbon atoms in neighbouring layers separated by the intercalate layer. At high fields spin-splitting is observed. The ratio of the spin to orbital splitting $\gamma = \frac{1}{2} gm^*/m_e$ equals 0.37 and 0.45 for $CuCl_2$ and $AlCl_{3.4}$, respectively, hence an enhanced value for the g-factor results. For a detailed analysis and a comparison with the band-structure model as proposed by Blinowski et al. [43] we refer to Ref. [42].

References

[1] R. Gersdorf, F.R. de Boer, J.C. Wolfrat, F.A. Muller and L.W. Roeland, in: High Field Magnetism, ed. M. Date (North-Holland, Amsterdam, 1983) p. 277.
[2] L.W. Roeland, R. Gersdorf and W.C.M. Mattens, Physica B 155 (1989) 58.
[3] R. Gersdorf, P.H. Frings, J.J.M. Franse and F.R. de Boer, Physica B 201 (1994) 530.
[4] R. Gersdorf, F.A. Muller and L.W. Roeland, Coll. Int. CNRS 166 (1967) 185.
[5] K. Bakker, Thesis, University of Amsterdam (1993).
[6] R. Verhoef, F.R. de Boer, J.J.M. Franse, C.J.M. Denissen, T.H. Jacobs and K.H.J. Buschow, J. Magn. Magn. Mater. 80 (1989) 41.
[7] R. Verhoef, R.J. Radwanski and J.J.M. Franse, J. Magn. Magn. Mater. 89 (1992) 176.
[8] J.P. Liu, F.R. de Boer, P.F. de Châtel, R. Coehoorn and K.H.J. Buschow, J. Magn. Magn. Mater., submitted.

[9] G.F. Zhou, X. Li, F.R. de Boer and K.H.J. Buschow, Physica B 177 (1992) 286; G.F. Zhou, X. Li, F.R. de Boer and K.H.J. Buschow, J. Magn. Magn. Mater. 109 (1992) 265.
[10] Z.G. Zhao, P.F. de Châtel, F.R. de Boer and K.H.J. Buschow, J. Appl. Phys. 73 (1993) 6522.
[11] Z.G. Zhao, X. Li, J.H.V.J. Brabers, P.F. de Châtel, F.R. de Boer and K.H.J. Buschow, J. Magn. Magn. Mater. 123 (1993) 74.
[12] Z.G. Zhao, N. Tang, F.R. de Boer, P.F. de Châtel, and K.H.J. Buschow, J. Magn. Magn. Mater., submitted.
[13] R. Verhoef, Thesis, University of Amsterdam (1990)
[14] D.C. Zeng, N. Tang, Q.A. Li, F.R. de Boer and K.H.J. Buschow, to be published.
[15] V. Sechovsky and L. Havela, in: Ferromagnetic Materials, Vol. 4, eds. E.P. Wohlfarth and K.H.J. Buschow (North-Holland, Amsterdam, 1988) p. 309.
[16] L. Havela, V. Sechovsky, F.R. de Boer, E. Brück and H. Nakotte, Physica B 177 (1992) 159.
[17] H. Nakotte et al. Physica B 201 (1994) 247.
[18] F. Mirambet, P. Gravereau, B. Chevalier, L. Trut and J. Etourneau, J. Alloys Comp. 191 (1993) L1.
[19] M.N. Peron et al., J. Alloys Comp., in press.
[20] R. Verhoef, A. de Visser, A. Menovsky, A.J. Riemersma and J.J.M. Franse, Physica B 142 (1986) 11.
[21] A. de Visser, A.A. Menovsky and J.J.M. Franse, Physica B 147 (1984) 81.
[22] K. Bakker, A. de Visser, A.A. Menovsky and J.J.M. Franse, Physica B 186–188 (1993) 687.
[23] J.J.M. Franse, K. Kadowaki, A. Menovsky, M. van Sprang and A. de Visser, J. Appl. Phys. 61 (1987) 3380.
[24] K. Bakker, A. de Visser, A.A. Menosky and J.J.M. Franse Phys. Rev. B 46 (1992) 544.
[25] C. Geibel et al., Z. Phys. B 84 (1991) 1.
[26] K. Gloos et al., Phys. Rev. Lett. 70 (1993) 501.
[27] A. Grauel et al., Phys. Rev. B 46 (1992) 5818.
[28] A. de Visser et al., Physica B 179 (1992) 84.
[29] A. de Visser et al., Physica B 186–188 (1993) 291.
[30] A. Krimmel et al., Z. Phys. B 86 (1992) 161.
[31] A. de Visser, H.P. van der Meulen, L.T. Tai and A.A. Menovsky, Physica B 199&200 (1994) 100.
[32] K. Sugiyama, T. Inoue, N. Sato, T. Komatsubara, A. Yamagishi and M. Date, Physica B 186–188 (1993) 723.
[33] C.P. Bean, Rev. Mod. Phys. 36 (1964) 31.
[34] A. Gerber, J.N. Li, Z. Tarnawski, J.J.M. Franse and A.A. Menovsky, Phys. Rev. B 47 (1993) 6047.
[35] J.N. Li et al., Physica C 169 (1990) 81.
[36] E.J. Kramer, J. Appl. Phys. 44 (1973) 1360.
[37] R.E. Enstrom and J.R. Appert, J. Appl. Phys. 43 (1972) 1915.
[38] J.N. Li, Thesis, University of Amsterdam (1992).
[39] M.S. Dresselhaus and G. Dresselhaus, Adv. Phys. 30 (1981) 139.
[40] V.V. Avdeev, V.Ya. Akim, N.B. Brandt, V.N. Davydov, V.A. Kulbachinskii and S.G. Ionov, Sov. Phys. JETP 67 (1988) 2496.
[41] V.A. Kulbachinskii, S.G. Ionov, S.A. Lapin and V.V. Avdeev, J. Physique 1-2 (1992) 1941.
[42] V.A. Kulbachinskii, S.G. Ionov, S.A. Lapin and A. de Visser, to be published.
[43] J. Blinowski, Nguyen Hy Hau, C. Rigaux, J.P. Vieren, R. Le Toullec, G. Furdin, A. Hérold and J. Melin, J. Physique 41 (1980) 47.